Facet-dependent NiO reduction revealed by surface-sensitive *in situ* scanning transmission electron microscopy

Yunduo Yao,[1] Chunhong Chen,[1] Xuyun Guo,[1] Longhai Zhang,[2] Changsheng Chen,[1] Zhiming Cui,[2] Xiangli Che,[1,*] and Ye Zhu[1,†]

[1]*Department of Applied Physics, Research Institute for Smart Energy, The Hong Kong Polytechnic University, Hong Kong, China*
[2]*School of Chemistry and Chemical Engineering, South China University of Technology, Guangzhou, Guangdong 510641, China*

(Received 14 January 2025; accepted 2 June 2025; published 2 July 2025)

In situ surface reduction has been widely adopted as an activation process on Ni-based catalysts, which can reduce NiO to highly active metallic Ni for catalysis. The detailed surface reduction mechanism and pathways, however, remain largely unclear. Here we present an *in situ* microscopic observation of the process of NiO surface reduction using surface-sensitive scanning transmission electron microscopy (STEM). The specially prepared NiO crystals with well-defined facet structure enable us to identify the facet-dependent reduction behavior: Reduced Ni nanoparticles preferentially exsolve on {111} facets of NiO surface initially, followed by particle growth and coalescence at higher temperature, and eventually migrate to {100} facets with higher binding energy to stabilize Ni nanoparticles. Remarkably, the formed Ni nanoparticles maintain the nearly epitaxial orientation relationship with the NiO matrix, with lattice mismatch accommodated by periodic edge dislocations at the Ni/NiO interface. Such facet-dependent reduction behavior is governed by the surface energies derived by density functional theory calculations. Besides shedding light on the fundamental mechanism of NiO surface reduction, our work also demonstrates a powerful approach combining surface-sensitive STEM with *in situ* capability to interrogate various physical and chemical processes on the surface.

DOI: 10.1103/zsrt-5txk

I. INTRODUCTION

Understanding the redox behavior of transition metals is important for both fundamental science and technological applications [1–5]. Especially in the form of nanomaterials, transition metals can exhibit remarkable redox reactivity, allowing them to be utilized as catalysts. Such metallic nanomaterials are often synthesized by reductive annealing of the corresponding oxides [6], or oxidized on the surfaces which requires reductive annealing to expose the active metallic sites [7]. As a typical example, nickel (Ni) is among the most efficient catalysts for the decomposition of NH_3 and nitric oxide [8–10]. Due to the susceptibility of Ni to oxidation, it is often prepared in the form of NiO, which requires *in situ* reductive annealing as an activation process to generate metallic Ni right before the catalytic reactions [10,11]. Reductive annealing has also been used to fabricate Ni-ceramic composite anodes for solid-oxide fuel cells [12], and Ni/NiO magnetic nanocomposites for spintronics [1]. The wide adoption of reductive annealing in Ni-based materials has incited numerous research works investigating the reduction mechanism [3,12–16]. *In situ* studies on the reduction of NiO to Ni have been carried out by transmission electron microscopy (TEM) under low oxygen (O_2) partial pressure in hydrogen (H_2), $CO + H_2$, CH_4, as well as vacuum annealing [3,12,13,15–17]. Various insights have been achieved, such as the mechanism of H_2 dissociation and adsorption that facilitates NiO reduction [16]. On the other hand, most of these studies focus on the bulk reduction behavior inside NiO, whereas the surface reduction behavior that is more relevant to catalysis has not yet been adequately explored. In particular, the preferential nucleation sites of the reduced Ni phase and its growth behavior on NiO surfaces are largely unknown, leaving a knowledge gap hindering the progress of mechanistic understanding and performance optimization of the subsequent catalytic reactions.

Probing the surface reduction behavior of NiO requires not only high-resolution microscopy techniques with both surface sensitivity and *in situ* capability, but also novel NiO materials with well-defined surface structure, rather than the conventionally studied round-shaped NiO nanoparticles. In this work, we utilize a backscattered electron (BSE) detector in scanning TEM (STEM) to realize high-resolution surface microscopy [18–20]. Combining with *in situ* heating, we apply such an *in situ* BSE-STEM approach on specially prepared NiO nanopolyhedra with distinct facets to reveal the surface reduction dynamics in real time at nanoscale. We discover the facet-dependent surface reduction behavior of NiO crystals, which can be well explained by the surface energies derived by density functional theory calculations. *Ex situ* STEM is also carried out at atomic scale to reveal the nearly epitaxial orientation relationship between the reduced Ni nanoparticles and the NiO matrix, with lattice mismatch accommodated by periodic edge dislocations at the Ni/NiO interface.

*Contact author: xiangli.che@polyu.edu.hk
†Contact author: yezhu@polyu.edu.hk

II. METHODS

A. Synthesis and characterization of {311}-faceted NiO

High-index faceted NiO was synthesized by the molten salt synthesis (MSS) method [21]. First, the decomposition of $Ni(NO_3)_2 \cdot 6H_2O$ (5 mmol) precursor was performed in the salt mixture of NaCl and KCl (1:1) using a 1:10 molar ratio of precursor to salt. Following being ground with a mortar and pestle for 20 min, the mixture was transferred to calcine at a heating rate of 2.5 °C/min to 550 °C and kept for 4 h in an oxygen (O_2) atmosphere. After cooling to room temperature, the product was cleaned and purified via water three times and via ethanol one time, and then put into a drying oven at 60 °C for at least 12 h.

X-ray diffraction (XRD) was conducted on a parallel-beam XRD instrument (Rigaku SmartLab 9 kW - Advance, with Cu $K\alpha$ of wavelength 1.5406 Å) at 45 kV and 200 mA. Scanning electron microscopy (SEM) images were recorded via field emission scanning electron microscope (Tescan MAIA3) at an accelerating voltage of 15 kV. TEM and selected area electron diffraction (SAED) were carried out on a field-emission transmission electron microscope (JEOL JEM-2100F) at 200 kV. The surface-sensitive backscattered-electron imaging was conducted in scanning transmission electron microscopy mode with a backscattered-electron detector (BSE-STEM) on the same TEM (JEOL JEM-2100F) at 200 kV.

B. *In situ* surface reduction

An *in situ* surface reduction experiment was performed using a heating holder (see Fig. S1(a) of the Supplemental Material [22]) system (Protochips, Fusion Select) assisted by the microelectromechanical systems (MEMS)-based thermal E-chip [Fig. S1(b)] [22] under a vacuum environment in STEM mode with a surface-sensitive backscattered-electron detector (BSE-STEM) at 200 kV on TEM (JEOL JEM-2100F). The E-chip was cleaned with Ar/O_2 (3:1) plasma for 1 min before dropping {311} faceted NiO ink composed of a uniform mixture of NiO (0.5 mg) and ethanol (2 mL) onto the integrated nine holes in the E-chips [Fig. S1(c)] [22]. After that, the E-chip was assembled onto the heating holder with a temperature profile for reduction process control [Fig. S1(d)] [22], where the temperature was set to be directly heated from 25 °C to 200 °C at a heating rate of 20 °C/min, and then continuously increased to 800 °C in steps of 100 °C at the same heating rate. At each step, the temperature was kept for 10–20 min for reaction and observation. After the reduction at 500 °C, high-angle annular dark field (HAADF), high-resolution STEM (HRSTEM) imaging, electron energy loss spectroscopy (EELS), and SAED were conducted on a JEOL JEM-ARM200CF Cs-corrected TEM/STEM at an accelerating voltage of 200 kV. STEM image simulations were carried out using the abTEM software package (version 1.05) [23].

C. Density functional theory calculation

All calculations were carried out using the Vienna Ab initio Simulation Package (VASP) [24]. The projector-augmented wave was used to define the interaction between ion cores and valence electrons [25]. The generalized gradient approximation of Perdew-Burke-Ernzerhof was utilized to determine the exchange-correlation potential [26]. Spin polarization was considered in all computations, and the Hubbard effective term was set to be 6.2 eV for a better description of Ni $3d$ electrons, which was adapted from the Materials Project database [27]. The cutoff energy was set to 520 eV, while the convergence threshold for the self-consistent field (SCF) and ion steps were set to be 1×10^{-5} eV and 0.05 eV $Å^{-1}$, respectively. The vacuum space of all investigated slab models was set to 15 Å to eliminate the interaction between neighboring slabs. $3 \times 3 \times 1$ Monkhorst-Pack sampled k points were used to integrate the Brillouin zone for the calculation of surface energies and oxygen vacancy formation energies [28], while the k points for calculating adsorption energies were set to be $1 \times 1 \times 1$. The surface energy (α) was determined by using the following equation:

$$\alpha = \frac{E_{\text{slab}} - nE_{\text{bulk}}}{2A},$$

where E_{slab} is the total energy of the slab, E_{bulk} is the energy of a bulk unit, n is the number of bulk units in the slab, and A is the surface area of the slab. The oxygen vacancy formation energy (E_{Ov}) was calculated by

$$E_{\text{Ov}} = E_{\text{slab-Ov}} + E_{\text{O}} - E_{\text{slab}},$$

where $E_{\text{slab-Ov}}$ is the energy of the slab with an oxygen vacancy and E_{O} is the energy of an oxygen atom, which was considered half of the energy of O_2. The binding energy was defined as

$$E_{\text{b}} = (E_{\text{cluster}} + E_{\text{slab}} - E_{\text{cluster/slab}})/N_{\text{cluster}},$$

where $E_{\text{cluster/slab}}$ and E_{cluster} represent the energies of cluster plus substrate and the cluster, respectively. N_{cluster} is the number of atoms in the cluster.

III. RESULTS AND DISCUSSION

Molten-salt synthesized NiO is in the form of single crystals with high purity as confirmed by XRD as well as electron diffraction [Fig. 1(a) and insets of Figs. 1(e) and 1(f)]. Through tuning surface energy via the molten-salt media (see Sec. II), the trapezohedral (TPH) NiO crystals with various exposed facets can be obtained, as revealed by SEM in Fig. 1(b). The Miller indices of the facets are illustrated in Fig. 1(d), which are determined consistently by both the electron diffraction [insets of Figs. 1(c), 1(e), and 1(f)] and the projected angles (Fig. S2 [22,29]). In particular, the largest exposed facets are {311} [30], in contrast to lower-index facets that are usually observed on NiO crystals. Such relatively high-index facets should offer higher reactivity than the stable low-index facets. However, with higher resolution of the surface-sensitive BSE-STEM compared to SEM, the {311} facets are resolved to be not atomically flat but consist of high-density nanoterraces as visualized in Fig. 1(c). Truncated edges and corners with the exposed narrow {221} facets and small {100} and {111} facets are also observed. Expanded BSE-STEM images around the {100} [Fig. 1(e)] and {111} facets [Fig. 1(f)] at the truncated corners further reveal that the high-density surface steps correspond to the low-index {100} and {111} facets only several nanometers

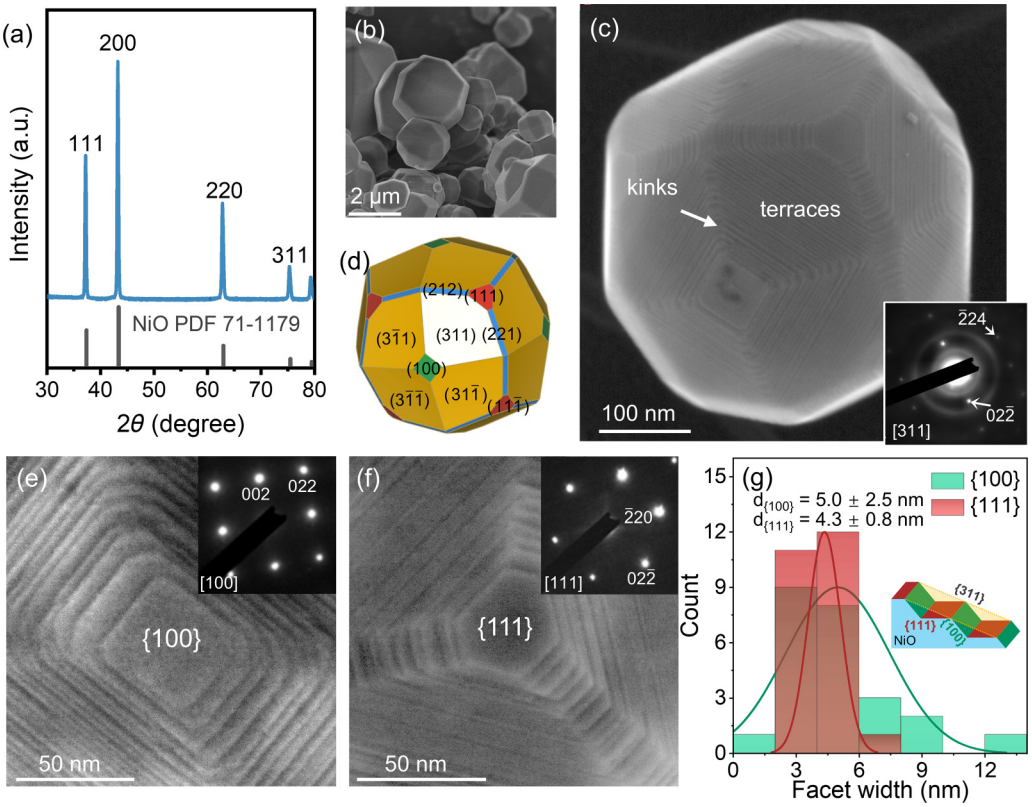

FIG. 1. (a) XRD, (b) SEM, and (c) BSE-STEM images from the molten-salt synthesized NiO crystals. The SAED pattern corresponding to the [311] zone axis is shown in the inset of (c). (d) Schematic model showing the faceted structure of the TPH NiO crystal imaged in (c). BSE-STEM images on the (e) {100} and (f) {111} facets at the truncated corners, with insets showing the corresponding SAED patterns. (g) Statistical width distribution of {100} and {111} nanosteps, which are organized with the average width ratio of ≈ 1.2 to form {311} facets as illustrated in the inset.

wide [Fig. 1(g)], which combine with the average width ratio of ≈1.2 to form the nanoterraced {311} facets [Fig. 1(g)]. We note that Susman *et al.* have observed the formation of {100} and {111} microfacets on NiO {311} facets, but only for ⩾ 850 °C synthesis temperature that gives rise to relatively large surface steps [26]. With lower synthesis temperatures such as 550 °C used in our work, the seemingly flat {311} facets were shown in their SEM images, just like in Fig. 1(b). With much enhanced image resolution of our BSE-STEM, Fig. 1 on the similarly synthesized NiO crystals clearly demonstrates that, even with 550 °C synthesis, {311} facets are still not flat at nanoscale, but composed of low-index {100} and {111} nanosteps that may not be resolvable by conventional SEM.

The achieved NiO crystals with well-characterized surface structure provide a unique system to study the mechanism of surface reduction and its dependence on various facets. We adopt *in situ* heating under high vacuum to simulate the low O_2 partial pressure for reductive annealing, and combine with surface-sensitive BSE-STEM to track the surface structure change in real time (Fig. S1 [22]). As shown in Fig. 2, upon heating to 300 °C, both {100} and {111} nanosteps show exsolved nanoparticles ≈7 nm in size [Figs. 2(b) and 2(h)], which are presumably Ni nanoparticles reduced from NiO. With increasing temperature, new nanoparticles emerge due to more exsolution, as indicated by blue arrows in Fig. 2(d). Meanwhile, the earlier exsolved nanoparticles grow larger with the total number decreasing, which can be attributed to coalescence and Oswald ripening processes at elevated temperature. Coalescence has been explicitly observed between the labeled nanoparticles 1–3 at 700 °C [Fig. 2(d)] and between 4 and 5 at 800 °C [Fig. 2(e)]. Interestingly, the observed coalescence mostly occurs on {111} nanosteps (such as nanoparticles 1–5), while nanoparticles on {100} nanosteps (such as nanoparticles 6 and 7) appear to be less mobile. The detailed particle counting further reveals the migration of nanoparticles from {111} nanosteps initially at 300 °C [Fig. 2(b)] to {100} nanosteps at 800 °C [Fig. 2(e)], as plotted in Fig. 2(g). Eventually at 800 °C, nanoparticles reach an average size of ≈ 20 nm [Fig. 2(h)], predominantly distributed on {100} nanosteps but close to the {100}/{111} intersections. We note that despite the exsolved nanoparticles, the NiO crystals maintain their size and TPH shape during *in situ* reduction up to 800 °C (Figs. 2(a) and 2(f); Figs. S3 and S4 [22]).

The exsolved nanoparticles are pure metallic Ni as confirmed by higher-resolution characterization in STEM. EELS of the Ni $L_{2,3}$ edges on the nanoparticles (with the NiO support) show the decreased L_3/L_2 ratio with increased signal between the L_3 and L_2 edges after reduction at 500 °C (Fig. S5 [22]), evidencing the reduced Ni valence in the formed nanoparticles [31]. Annular dark-field (ADF) STEM imaging

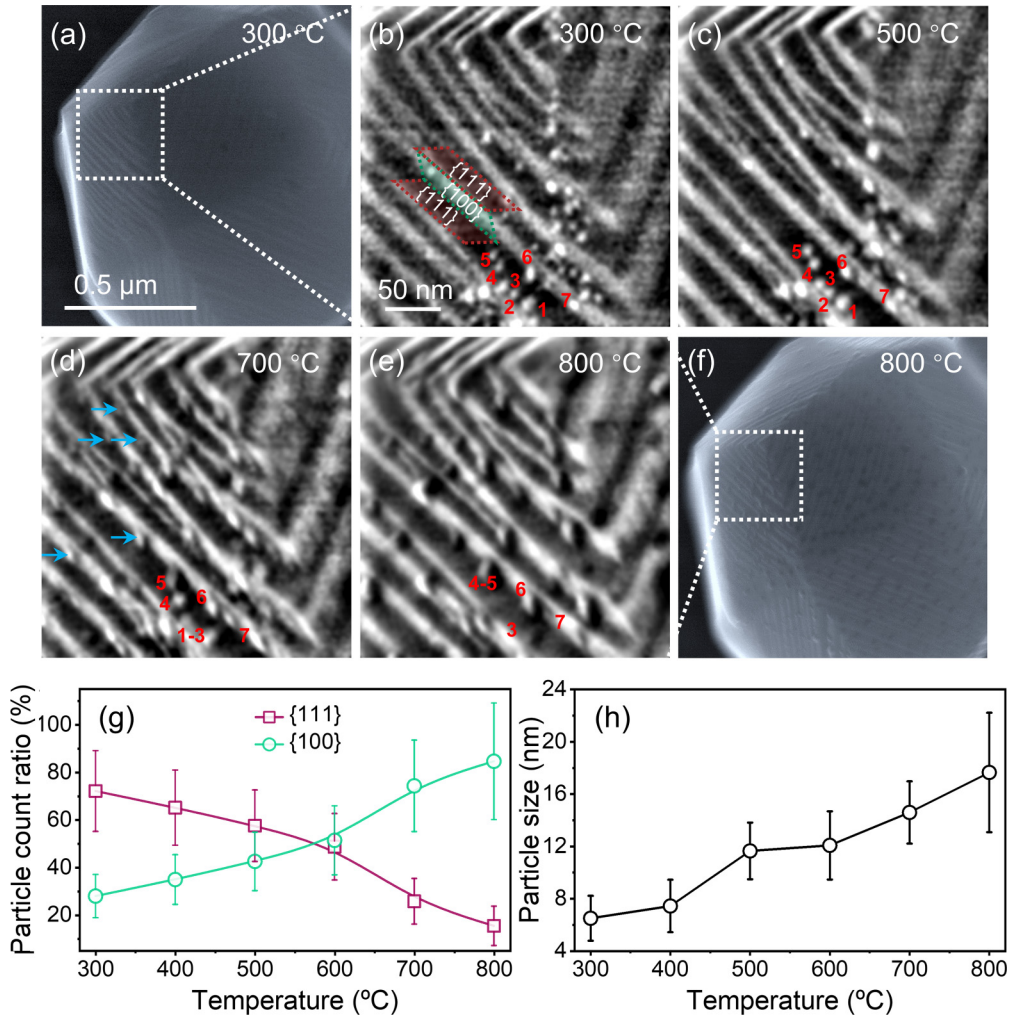

FIG. 2. [(a)–(f)] *In situ* BSE-STEM observation of NiO facets with expanded images at various temperatures shown in (b)–(e). (g) Particle count ratio and (h) particle size measured from *in situ* BSE-STEM observation at various temperatures.

at atomic scale reveals a moiré pattern resulting from the lattice overlap between nanoparticles and the NiO support [Figs. 3(b) and 3(e)], which is consistent with SAED showing satellite diffraction spots [Figs. 3(c) and 3(g)]. Detailed analysis further shows that the SAED patterns in Figs. 3(c) and 3(g) are formed by superposition of NiO (red circles) and Ni (green circles) diffraction patterns, both at the same zone axes ([011] and [100]), while other satellite spots are attributed to double diffraction with considerably weak intensity compared to the main diffraction spots, as illustrated by the schematics in Figs. 3(d) and 3(h). It unambiguously demonstrates that the exsolved nanoparticles are metallic Ni grown on NiO nanofacets with the epitaxial orientation relationship $\langle 100\rangle_{\mathrm{Ni}}||\langle 100\rangle_{\mathrm{NiO}}$, $\langle 011\rangle_{\mathrm{Ni}}||\langle 011\rangle_{\mathrm{NiO}}$, and $\{111\}_{\mathrm{Ni}}||\{111\}_{\mathrm{NiO}}$. STEM image simulations have been further carried out to validate the observed moiré patterns (Fig. S6 [22]). On the other hand, the acquired Ni diffraction spots are all extended to short streaks [Figs. 3(c) and 3(g)], indicating small orientation variations of the Ni nanoparticles, which deviate from the perfect epitaxial growth. Figure 3(e) also reveals that the moiré pattern is terminated by {100} and {110} lattice planes, which define the edges of the formed Ni nanoparticles with presumably minimized surface energy. Along these particle edges, periodic edge dislocations can be identified with Burgers vector $\mathbf{b} = 1/2\langle 001\rangle$ and regular spacing ≈1.06 nm [Fig. (3e)]. This way, six $\{002\}_{\mathrm{Ni}}$ lattice fringes on the left side of Fig. 3(e) correspond to five $\{002\}_{\mathrm{NiO}}$ fringes on the right, which effectively accommodates the ≈16% lattice mismatch between Ni ($a = 3.52$ Å) and NiO ($a = 4.17$ Å) while maintaining the nearly epitaxial orientation relationship. Our observation of near-epitaxial growth of metallic Ni on NiO crystals, with well-defined morphology and orientation relationship, is largely consistent with the reported Ni/NiO nanocomposites prepared by vacuum reduction of NiO films [1], suggesting its wide presence during the reduction process on the NiO surface.

It is noted that, instead of continuous beam exposure, the electron beam was mostly blanked during *in situ* heating to minimize the potential beam effects. We have also examined regions not being tracked during *in situ* observation: The exsolution of surface Ni particles are consistently seen after heating at 500 °C (Fig. S4(d) [22]), validating that the

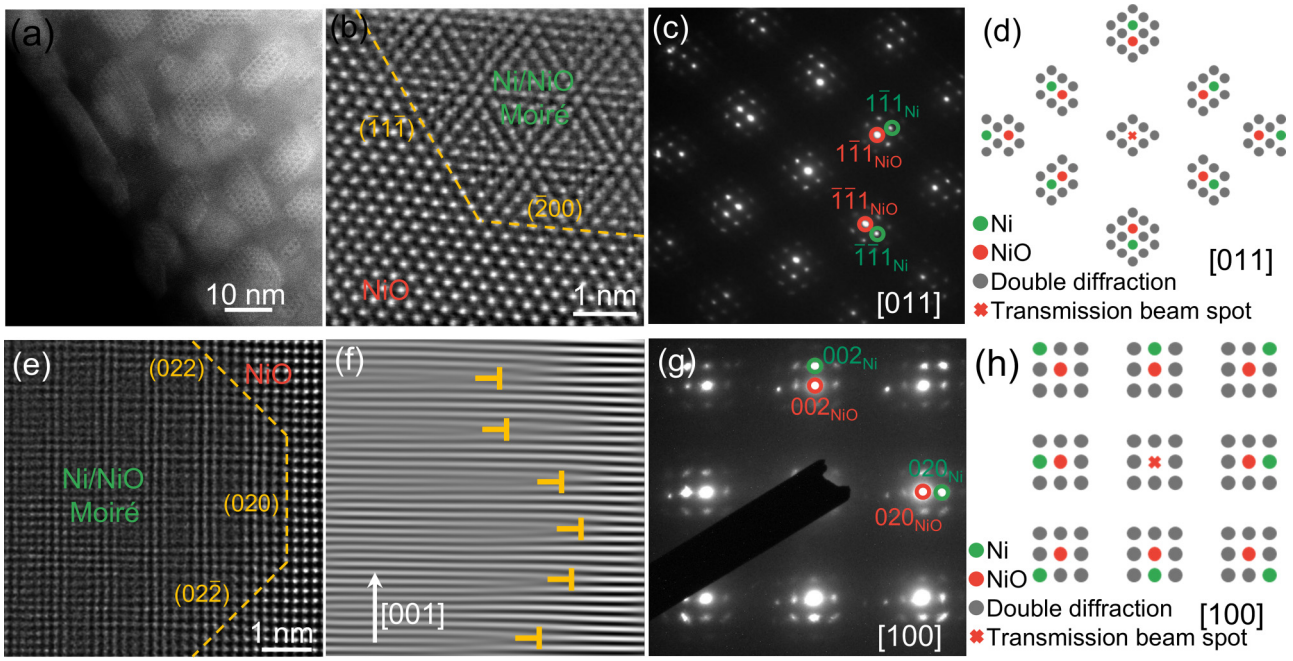

FIG. 3. (a) Low-magnification and (b) atomic-resolution annular dark field (ADF)-STEM images, (c) SAED pattern, and (d) the corresponding schematic for the edge of [011]-oriented NiO after reduction at 500 °C. (e) Atomic-resolution ADF-STEM image and (f) the corresponding Fourier-filtered image showing (002) lattice fringes, (g) SAED pattern, and (h) the corresponding schematic for the edge of [100]-oriented NiO after reduction at 500 °C.

observed surface reduction is due to reductive heating rather than the beam effects.

To better understand the observed surface reduction behavior, we have conducted density functional theory (DFT) calculations to compare various energies associated with {100} and {111} facets of NiO (see atomic models in Fig. S7 [22]), as listed in Table I. It enables us to paint a comprehensive picture of the surface reduction process on faceted NiO crystals, as illustrated in Fig. 4: During initial reduction, oxygen atoms escape from NiO surfaces and metallic Ni nanoparticles start to nucleate. More Ni nanoparticles form on {111} facets [Fig. 2(g)], which can be attributed to their higher surface energy (3.60 J/m^2) and lower oxygen vacancy (O_v) formation energy (0.02 eV) than {100} facets (0.84 J/m^2 and 4.60 eV). Further increasing temperature leads to the growth and coalescence of Ni nanoparticles, the latter of which mostly occurs on {111} facets, also consistent with their lower binding energy with metallic Ni. Eventually, the ripened Ni nanoparticles migrate to the intersections of {100} and {111} facets, with more contact on {100} facets due to their higher binding energy with metallic Ni (2.44 eV/atom) compared with {111} facets (0.64 eV/atom). In particular, the nearly epitaxial orientation relationship identified between Ni and NiO suggests that when oxygen escapes, the remaining Ni sublattice on the surface maintains its face-centered-cubic structure with the same orientation as the NiO matrix. Even after Ni nanoparticles exsolve from the surface and grow to larger size, their lattice orientation is largely preserved, with the lattice mismatch accommodated by the periodic edge dislocations at the Ni/NiO interface.

TABLE I. Surface energies, O_v formation energies, and binding energies for the system of Ni on NiO {100} and {111} facets from DFT calculation.

	Surface energy (J/m^2)	O_v formation energy (eV)	Binding energy (eV/atom)
{100}	0.84	4.60	2.44
{111}	3.60	0.02	0.64

IV. CONCLUSIONS

In summary, we have synthesized NiO crystals with exposed large {311} facets composed of {100} and {111} nanosteps on the surface. *In situ* reduction on such faceted NiO leads to the exsolution of metallic Ni nanoparticles preferentially on {111} nanosteps initially, consistent with their higher surface energy and lower O_v formation energy as evinced by DFT calculations. Ni nanoparticles grow and coalesce at higher temperatures, and eventually migrate to {100} facets that have higher binding energy to stabilize Ni nanoparticles. Remarkably, the formed Ni nanoparticles maintain the nearly epitaxial orientation relationship with the NiO matrix, with the lattice mismatch accommodated by the periodic edge dislocations at the Ni/NiO interface. Our work indicates that for catalytic reactions that need active Ni atoms, the {111} NiO surface may be preferred, which can be easily reduced to generate more Ni sites with higher activity, whereas for applications that require more stable Ni phases, such as spintronics with ferromagnetic Ni and antiferromagnetic NiO nanocomposites, {100} NiO is more suitable to stabilize the metallic Ni phase. Besides unraveling the surface reduction behavior

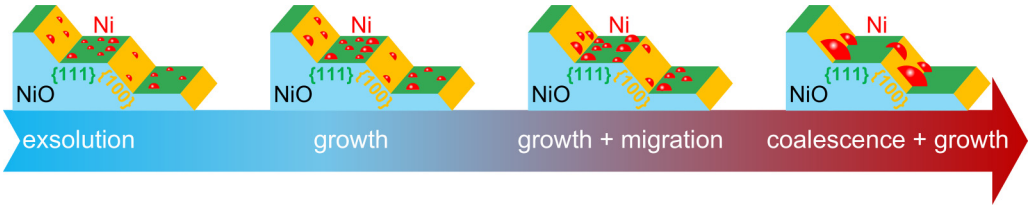

FIG. 4. Schematic of the surface reduction pathway on faceted NiO crystals.

of NiO crystals, our work also demonstrates a powerful approach combining surface-sensitive BSE-STEM with *in situ* capability to explore physical and chemical processes on the surface.

ACKNOWLEDGMENTS

This work was financially supported by the Research Grants Council of Hong Kong (General Research Fund No. 15307522) and the Hong Kong Polytechnic University (Grant No. ZVRP).

Y.Y., C.C., and X.G. contributed equally to this work.

DATA AVAILABILITY

The data supporting this study's findings are available within the article.

[1] X. Wang, Z. Qi, J. Liu, H. Wang, X. Xu, X. Zhang, and H. Wang, Strong interfacial coupling of tunable Ni–NiO nanocomposite thin films formed by self-decomposition, ACS Appl. Mater. Interfaces **13**, 39730 (2021).

[2] A. P. LaGrow, L. Sinatra, A. Elshewy, K.-W. Huang, K. Katsiev, A. R. Kirmani, A. Amassian, D. H. Anjum, and O. M. Bakr, Synthesis of copper hydroxide branched nanocages and their transformation to copper oxide, J. Phys. Chem. C **118**, 19374 (2014).

[3] A. P. LaGrow, N. M. Alyami, D. C. Lloyd, O. M. Bakr, E. D. Boyes, and P. L. Gai, *In situ* oxidation and reduction of triangular nickel nanoplates via environmental transmission electron microscopy, J. Microscopy **269**, 161 (2018).

[4] Y. Zeng, Y. Meng, Z. Lai, X. Zhang, M. Yu, P. Fang, M. Wu, Y. Tong, and X. Lu, An ultrastable and high-performance flexible fiber-shaped Ni–Zn battery based on a Ni–NiO heterostructured nanosheet cathode, Adv. Mater. **29**, 1702698 (2017).

[5] S. Apergi, G. Brocks, and S. Tao, Tuning the electronic levels of NiO with alkali halides surface modifiers for perovskite solar cells, Phys. Rev. Mater. **4**, 085403 (2020).

[6] H. Y. Kim, H. M. Lee, R. G. S. Pala, V. Shapovalov, and H. Metiu, CO oxidation by rutile TiO_2 (110) doped with V, W, Cr, Mo, and Mn, J. Phys. Chem. C **112**, 12398 (2008).

[7] J. L. Cao, Z. L. Yan, Q. F. Deng, Z. Y. Yuan, Y. Wang, G. Sun, X. D. Wang, B. Hari, and Z. Y. Zhang, Homogeneous precipitation method preparation of modified red mud supported Ni mesoporous catalysts for ammonia decomposition, Catal. Sci. Technol. **4**, 361 (2014).

[8] F. Schüth, R. Palkovits, R. Schlögl, and D. S. Su, Ammonia as a possible element in an energy infrastructure: Catalysts for ammonia decomposition, Energy Environ. Sci. **5**, 6278 (2012).

[9] Z.-W. Wu, J. Xiong, C.-W. Wang, and Y.-H. Qin, Supporting high-loading Ni on SBA-15 as highly active and durable catalyst for ammonia decomposition reaction, Int. J. Hydrogen Energy **48**, 4728 (2023).

[10] J. Zhang, H. Xu, and W. Li, Kinetic study of NH_3 decomposition over Ni nanoparticles: The role of La promoter, structure sensitivity and compensation effect, Appl. Catal. A **296**, 257 (2005).

[11] H. Liu, Y. Zhang, S. Liu, S. Li, and G. Liu, Ni-CeO_2 nanocomposite with enhanced metal-support interaction for effective ammonia decomposition to hydrogen, Chem. Eng. J. **473**, 145371 (2023).

[12] J. Basu and R. Divakar, *In-situ* electron microscopy investigation of reduction-induced microstructural changes in NiO, Ceram. Int. **41**, 12658 (2015).

[13] S. Ogawa, R. Taga, A. Yoshigoe, and Y. Takakuwa, Two-step model for reduction reaction of ultrathin nickel oxide by hydrogen, J. Vac. Sci. Technol. A **39**, 043207 (2021).

[14] Y. Yao, G. Zhao, X. Guo, P. Xiong, Z. Xu, L. Zhang, C. Chen, C. Xu, T.-S. Wu, Y.-L. Soo, Z. Cui, M. M.-J. Li, and Y. Zhu, Facet-dependent surface restructuring on nickel (oxy)hydroxides: A self-activation process for enhanced oxygen evolution reaction, J. Am. Chem. Soc. **146**, 15219 (2024).

[15] F. Maglia, G. Spinolo, and U. Anselmi-Tamburini, Mechanism of low temperature decomposition of NiO single crystals, Solid State Sci. **11**, 1686 (2009).

[16] Q. Jeangros, T. W. Hansen, J. B. Wagner, C. D. Damsgaard, R. E. Dunin-Borkowski, C. Hébert, J. Van herle, and A. Hessler-Wyser, Reduction of nickel oxide particles by hydrogen studied in an environmental TEM, J. Mater. Sci. **48**, 2893 (2013).

[17] S. Chenna and P. A. Crozier, *In situ* environmental transmission electron microscopy to determine transformation pathways in supported Ni nanoparticles, Micron **43**, 1188 (2012).

[18] Y. Zhu, H. Inada, K. Nakamura, and J. Wall, Imaging single atoms using secondary electrons with an aberration-corrected electron microscope, Nat. Mater. **8**, 808 (2009).

[19] S. Hwang, L. Wu, K. Kisslinger, J. Yang, R. Egerton, and Y. Zhu, Secondary-electron imaging of bulk crystalline specimens in an aberration corrected STEM, Ultramicroscopy **261**, 113967 (2024).

[20] D. R. G. Mitchell and G. Casillas, Secondary electron imaging in an aberration-corrected STEM, Microsc. Today **24**, 22 (2016).

[21] M. D. Susman, H. N. Pham, X. Zhao, D. H. West, S. Chinta, P. Bollini, A. K. Datye, and J. D. Rimer, Synthesis of NiO crystals exposing stable high-index aacets, Angew. Chem. Int. Ed. **59**, 15119 (2020).

[22] See Supplemental Material at http://link.aps.org/supplemental/10.1103/zsrt-5txk for additional information on the *in situ* surface reduction experimental system, identification of the Miller index of the NiO trapezohedron, BSE-STEM images from 400 °C to 700 °C, EELS spectra, simulated STEM images, and the models of DFT calculation, which also contains Refs. [23,29].

[23] J. Madsen and T. Susi, The abTEM code: transmission electron microscopy from first principles, Open Res. Eur. **1**, 24 (2021).

[24] G. Kresse and J. Furthmüller, Efficient iterative schemes for *ab initio* total-energy calculations using a plane-wave basis set, Phys. Rev. B **54**, 11169 (1996).

[25] P. E. Blöchl, Projector augmented-wave method, Phys. Rev. B **50**, 17953 (1994).

[26] J. P. Perdew, K. Burke, and M. Ernzerhof, Generalized gradient approximation made simple, Phys. Rev. Lett. **77**, 3865 (1996).

[27] A. Jain, S. P. Ong, G. Hautier, W. Chen, W. D. Richards, S. Dacek, S. Cholia, D. Gunter, D. Skinner, G. Ceder, and K. A. Persson, Commentary: The materials project: A materials genome approach to accelerating materials innovation, APL Mater. **1**, 011002 (2013).

[28] H. J. Monkhorst and J. D. Pack, Special points for Brillouin-zone integrations, Phys. Rev. B **13**, 5188 (1976).

[29] Z. Quan, Y. Wang, and J. Fang, High-index faceted noble metal nanocrystals, Acc. Chem. Res. **46**, 191 (2013).

[30] M. D. Susman, H. N. Pham, D. West, S. Chinta, A. K. Datye, and J. D. Rimer, High-index NiO particle synthesis in alkali chloride salts: Nonclassical crystallization pathways and thermally-induced surface restructuring, Small **20**, 2308166 (2024).

[31] F. Lin, D. Nordlund, T.-C. Weng, Y. Zhu, C. Ban, R. M. Richards, and H. L. Xin, Phase evolution for conversion reaction electrodes in lithium-ion batteries, Nat. Commun. **5**, 3358 (2014).